


Photocatalytic Degradation of the Rhodamine B Dye Under Visible Light Using $\text{Ni}_x\text{Cu}_{(1-x)}\text{Fe}_2\text{O}_4$ Synthesized by EDTA-Citrate Complexation Method

Ila G. D. D. de Azevedo^{a*} , Matheus V. Rodrigues^a, Yara F. Gomes^b, Camila P. B. de Araújo^a,
Carlson P. de Souza^{a,b}, André L. L. Moriyama^a

^aUniversidade Federal do Rio Grande do Norte (UFRN), Programa de Pós-Graduação em Engenharia Química, Natal, RN, Brasil.

^bUniversidade Federal do Rio Grande do Norte (UFRN), Programa de Pós-Graduação em Ciência e Engenharia de Materiais, Natal, RN, Brasil.

Received: January 16, 2023; Revised: April 18, 2023; Accepted: June 27, 2023

The $\text{Ni}_x\text{Cu}_{(1-x)}\text{Fe}_2\text{O}_4$ ($x = 0, 0.2, 0.8, 1$) mixed nickel and copper ferrites were synthesized using the EDTA-Citrate complexation method and calcined at 700°C. The structure, properties and characterization of the samples were analyzed by DRX, Rietveld refinement, SEM, and DRE UV-Vis, indicating the phase formation of tetragonal (CuFe_2O_4 and $\text{Ni}_{0.8}\text{Cu}_{0.2}\text{Fe}_2\text{O}_4$) and cubic ($\text{Ni}_{0.8}\text{Cu}_{0.2}\text{Fe}_2\text{O}_4$ and NiFe_2O_4). The materials exhibited morphologies suitable for photocatalytic applications and a UV-Vis absorption range near 2 eV as expected for spinel ferrites. These materials were evaluated as photocatalysts for the degradation of Rhodamine B dye under heterogeneous photocatalysis conditions, simulating solar light irradiation, air injection, and different pH levels (2, 6, and 10). The results showed that the catalytic efficiency was higher for samples with a higher copper content and in a basic medium. Therefore, $\text{Ni}_x\text{Cu}_{(1-x)}\text{Fe}_2\text{O}_4$ mixed ferrites have promising potential as photocatalysts.

Keywords: Mixed nickel and copper ferrites, EDTA-Citrate, heterogeneous photocatalysis, Rhodamine B.

1. Introduction

One of the biggest problems of high industrialization is the pollution of the environment, which causes profound damage to nature in its most diverse environments. Dyes are soluble substances that assign or modify the color of a substrate, commonly used in various industrial segments such as the textile, tanning, paper, and pharmaceutical industries, among others¹. Rhodamine B is a synthetic dye from the xanthenes group, with solubility in different solvents, with multifunctionality and being used in several industries². The dyes are mostly synthetic, have an organic nature, stability to light and temperature, resistance to water and detergents, showing resistance to conventional effluent treatments, which allows the occurrence of contamination in aquatic environments, promoting inhibition of the penetration of light into water, large variations in chemical and biochemical oxygen demand, temperature elevation, pH variations, among others, directly affecting the aquatic biota³.

Therefore, it is necessary to use more efficient effluent treatments, such as Advanced Oxidative Processes (AOP's), where the total mineralization of most organic pollutants occurs⁴. Among them, there is the heterogeneous photocatalysis that consists of using a light source and a photocatalyst that remains suspended in the solution, the catalyst needs to have semiconductor properties to be activated by a light source due to the small bandgap, causing an electronic transition

and consequently the generation of oxidizing and reducing sites capable of catalyzing chemical reactions, degrading organic components^{5,6}.

Semiconductor catalysts can have different natures, including ferrites, which are magnetic ceramic materials with a crystalline structure and general formula MFe_2O_4 , where M represents transition metal cations and can be present in varied compositions⁷. Ferrites are promising semiconductors due to their low bandgap range 1.1 to 2.3 eV, as well as being easily separated due to their magnetic properties⁸. Nickel ferrite stands out due to its completely inverted spinel structure, presenting excellent magnetic properties, while copper ferrite presents a mixture in its spinel, configuring semiconductor properties, in this way the substitution of nickel in copper causes changes in the material properties, such as electrical resistivity, magnetic permeability, among others^{9,10}. Nickel and copper ferrites began to be studied a short time ago, however, they have already shown effective applications in antimicrobial activities⁹, gas sensor¹¹, material for lithium batteries¹², application in micro-sensors waves¹³ and mainly photocatalytic activities^{10,14}.

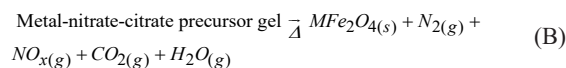
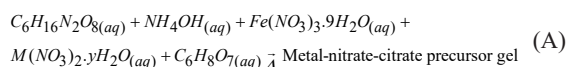
In view of this, this work used nickel and copper ferrites ($\text{Ni}_x\text{Cu}_{(1-x)}\text{Fe}_2\text{O}_4$), in different compositions ($x = 0; 0.2; 0.8; 1$), synthesized by the method of combined complexation EDTA-Citrate, to evaluate the effect on the photocatalytic degradation of the dye Rhodamine B, varying the pH of the solution, simulating effluents from textile industries.

*e-mail: ila.azevedo.079@ufrn.edu.br

2. Materials and Methods

2.1. Synthesis of ferrites $Ni_x Cu_{(1-x)} Fe_2 O_4$

The $Ni_x Cu_{(1-x)} Fe_2 O_4$ powders ($x = 0; 0.2; 0.8$ and 1), called x0, x20, x80, x100, were synthesized by the EDTA-citrate complexation method¹⁵ through the following procedure: Acid EDTA ($C_{10} H_{16} N_2 O_8$, 99.4%, Synth) was diluted in ammonium hydroxide ($NH_4 OH$, 27%, Synth) in the proportion of 1g:10mL under stirring and temperature controlled (40 °C) for 15 minutes, solution 1. Then, $Fe(NO_3)_3 \cdot 9H_2 O$ (98%, Sigma Aldrich), $Ni(NO_3)_2 \cdot 6H_2 O$ (97%, Isifar) and $Cu(NO_3)_2 \cdot 9H_2 O$ (98%, Synth), respectively, were added to Solution 1, in a stoichiometric amount referring to each composition, maintaining constant temperature and agitation for 15 minutes, resulting in Solution 2. Citric acid ($C_6 H_8 O_7$, 99.5%, Synth) was added to Solution 2, $NH_4 OH$ was used to adjust the pH to 9, and the temperature was increased (80 °C), the solution was kept under these conditions until the formation of the organometallic gel. The gel underwent a thermal pre-treatment at 230 °C for 180 minutes in order to eliminate the water and ammonium hydroxide still present in excess in the gel, giving rise to precursors $Ni_x Cu_{(1-x)} Fe_2 O_4$, which were subsequently subjected to a heat treatment to obtain the final powders at 700 °C for 240 minutes. The molar ratio of EDTA acid, citric acid and metallic ions used for the synthesis of ceramic powders was 1:1.5:1, respectively. Equations (A) and (B), based on¹⁶, generically express the chemical reactions occurring during the processes.



Where M = Ni or Cu or Ni/Cu and y = 6 for Ni and y = 3 for Cu.

2.2. Characterizations

X-ray diffractograms (XRD) were used to analyze the behavior and evolution of crystallographic phases of $Ni_x Cu_{(1-x)} Fe_2 O_4$. Measurements were obtained with a Shimadzu DRX-7000 diffractometer, using Cu-K α ($\lambda = 1.5406 \text{ \AA}$). The generated diffractograms present values of 2θ ranging from 10 to 70 degrees. The phases found were analyzed using the X'pert program, while the parameters and lattice position were determined using the Rietveld refinement method and were analyzed by the Structure Analysis System (GSAS2) with the EXPGUI graphical interface program.

Scanning electron microscopy measurements with field emission cannon (FEG-SEM) were performed in a FESEM equipment (Auriga, Carl Zeiss, USA), model Supra 35-VP equipped with a Bruker EDS detector (XFlash 410- M).

Diffuse reflectance spectroscopy (DRE) measurements were recorded at room temperature on a UVVis NIR spectrometer (Cary, model 5G) in the range 200-800 nm. Barium sulfate ($BaSO_4$) was used as a reference sample.

2.3. Photocatalytic activities

The activities of $Ni_x Cu_{(1-x)} Fe_2 O_4$ (x0, x20, x80 and x100), via heterogeneous photocatalysis, were evaluated

using solutions prepared with rhodamine B (RhB) 10 ppm, using an OSRAM ULTRA-VITALUX 300 W lamp, whose tungsten filament generates radiation similar to the solar spectrum. The system was maintained at room temperature (25 °C) and constant agitation, with the aid of an air purge. To study the effectiveness of the materials produced, tests were carried out with each type of catalyst, varying the nickel concentration (x0, x20, x80 and x100), as well as the pH^{2,6,10}, while the catalyst loads were equally distributed in all tests (0.62 g/L). All reactions were carried out for 240 minutes, with collection of samples of the solution at intervals of 30 minutes, the catalyst was separated by a magnet and the concentration was evaluated using a UV-Vis spectrophotometer with a wavelength of 556nm.

As all the experiments were carried out during a period of 4 hours, a "t student" test was applied to precisely define the order of the reaction¹⁷ identifying the kinetic behavior of the degradations with the objective of completing quantitative data of the activities photocatalytic properties of $Ni_x Cu_{(1-x)} Fe_2 O_4$ samples.

As the volume of the system is constant and the concentrations of the reagents are very small, we considered $C_A = C_B$.

$$\text{Assuming: } X_A = 1 - \frac{C_A}{C_{A0}} \quad (C)$$

$$\text{For first-order reactions: } -\ln \frac{C_A}{C_{A0}} = k.t \quad (D)$$

$$\text{For second-order reactions: } \frac{X_A}{1 - X_A} = C_{A0}.k.t \quad (E)$$

To test the models for pH variations^{2,6,10}, both kinetics (first and second order) were plotted.

When the correlation coefficients (R) are high for both models, a "t student" test is used to test the significance (F), with 95% confidence ($t^*_{exp} = 1.895$) that the linear coefficient (b) of the equation of the line is not statistically different from zero, where SE is the standard error.

$$t^* = \frac{|b-0|}{SE(b)} \quad (F)$$

If $t^*_1 > t^*_{exp}$ e $t^*_2 < t^*_{exp}$ then the second-order model is accepted.

3. Results and Discussions

Figure 1 shows the results of the $Ni_x Cu_{(1-x)} Fe_2 O_4$ diffractograms (x0, x20, x80 and x100). For x0 and x20, the presence of the main characteristic peaks of the tetragonal spinel structure (JCPDS n° 34-0425) with space group I41/amd characterizing the copper ferrite structure is observed. The insertion of Ni in the $CuFe_2 O_4$ structure (x20) caused the shift of the most intense peak (211) to the left, making it less symmetrical and indicating the presence of a tail to the left of the central point of the peak, as well as causing the displacement to the right of the peaks (103) and (202), being in greater intensity for the first one. This phenomenon can occur either by the presence of another crystalline phase next to the structure, or by punctual defects present in the crystalline structure, in this case caused

by the insertion of nickel in the CuFe_2O_4 matrix as reported by¹³. Since no other structure was detected besides the one mentioned, it is concluded by the second effect.

For x80 and x100, the presence of the main characteristic peaks of the cubic spinel structure (JCPDS n° 74-2081) with space group Fd-3m characterizing the nickel ferrite structure was also observed. The insertion of copper did not cause a significant change in the width of the peaks of the cubic structure of NiFe_2O_4 , only their displacement, indicating the expansion of the crystalline lattice, as shown by the calculation of the lattice parameter of 8.339 for x100 and

8.348 for x80, caused by the difference in ionic radius of Cu^{2+} and Ni^{2+} (0.73 and 0.72, respectively).

Using X-ray diffraction data and the Scherrer Equation (G), the size of the ferrite crystallites was estimated with an average value of 51.59 nm, 47.53 nm, 81.75 nm and 75.43 nm, in order x0, x20, x80 and x100, respectively. It was evaluated that the addition of nickel at 20% (x20) to copper ferrite causes a decrease in the average crystallite size, in reaction to pure copper ferrite (x0). While for pure nickel ferrite (x100) compared to with copper addition (x80), there was an increase in the average crystallite size.

$$L = \frac{0,9 * \lambda}{\beta \cos \theta} \quad (\text{G})$$

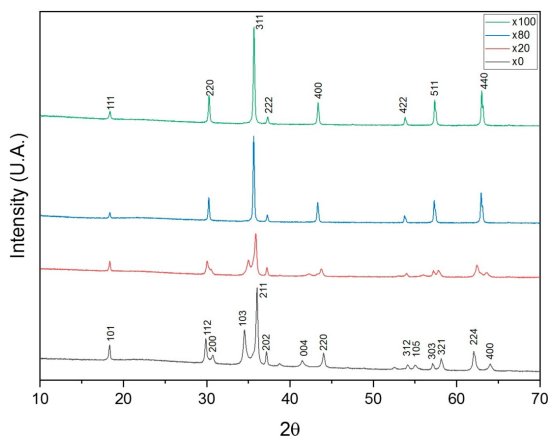


Figure 1. XRD patterns of synthesized $\text{Ni}_x\text{Cu}_{(1-x)}\text{Fe}_2\text{O}_4$ nanocrystals.

Figure 2 presents the refinements for the synthesized $\text{Ni}_x\text{Cu}_{(1-x)}\text{Fe}_2\text{O}_4$ nanocrystals, according to the diffractograms for x0 (2-A) and x20 (2-B), where the presence of the main characteristic peaks of the tetragonal spinel structure (JCPDS n° 34-0425) with space group 141/amd characterizing the copper ferrite structure, CIF chart n° 9011012 obtained through the Crystallography Open Database (COD) was used for the refining of 2-A and 2-B. For the x80 (2-C) and x100 (2-D) diffractograms, the presence of the main characteristic peaks of the cubic spinel structure (JCPDS n° 74-2081) with space group Fd-3m characterizing the nickel ferrite structure was observed, confirmed in the refinements presented, for the refinements, CIF letter No. 2300289 obtained through the Crystallography Open Database (COD) was used. Refinement was performed using a scale

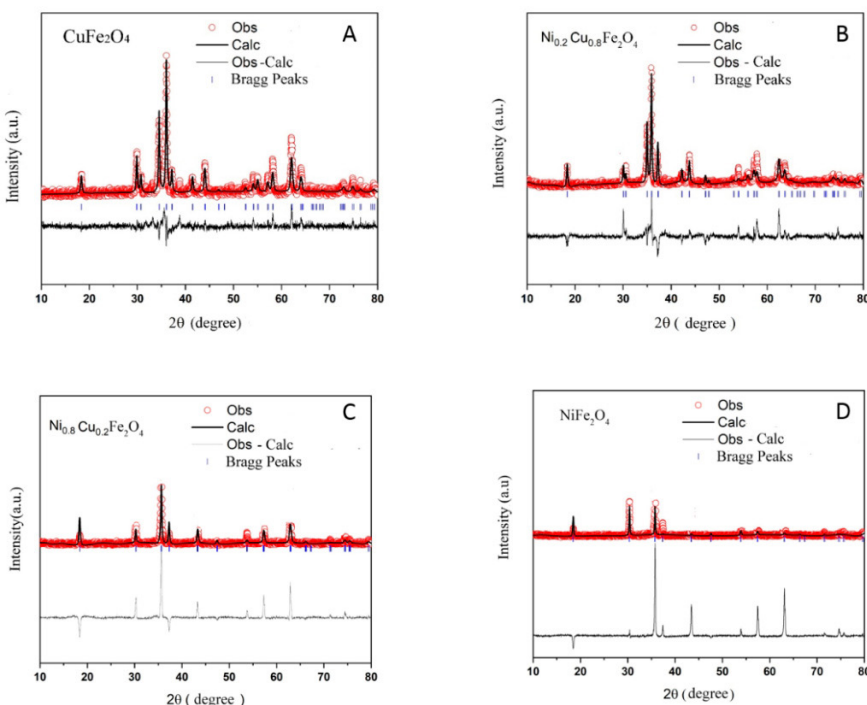


Figure 2. Observed (obs.) and theoretical (calculated) diffractograms for samples of $\text{Ni}_x\text{Cu}_{(1-x)}\text{Fe}_2\text{O}_4$ nanocrystals. (A) x0, (B) x20, (C) x80 and (D) x100.

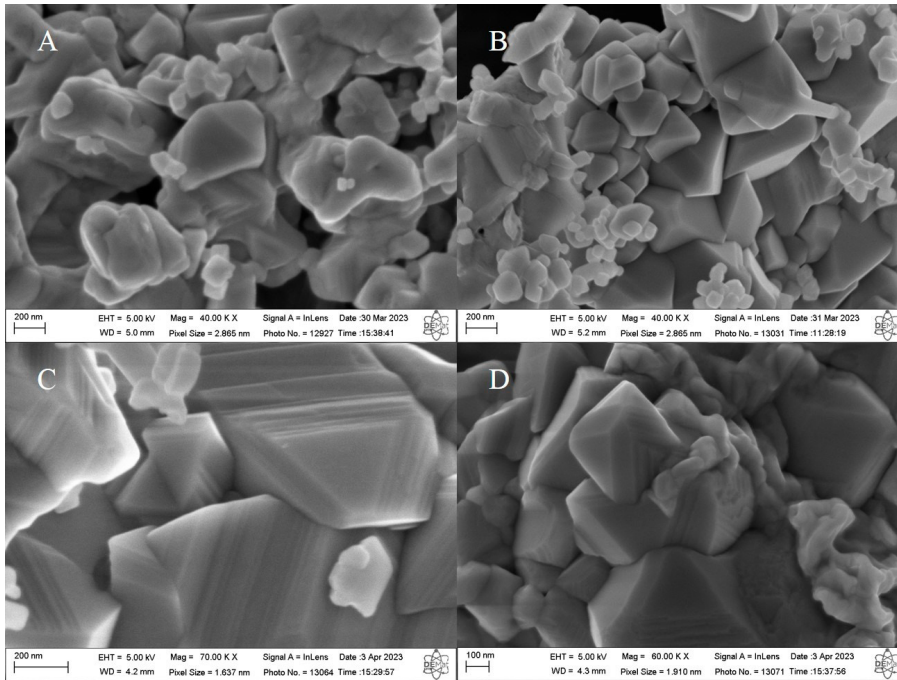


Figure 3. Scanning electron microscopy for $\text{Ni}_x\text{Cu}_{(1-x)}\text{Fe}_2\text{O}_4$ samples, x0(A), x20 (B), x80 (C), x100 (D).

factor, phase fraction, Chebyshev polynomial function for background, Thomson–Cox-Hasting pseudo-Voigt peak format, changes in lattice parameters, atomic fraction coordinates and isotropic thermal parameters as quality parameters. In Figure 2, we can observe the observed (obs.) and theoretical (calculated) refinement data obtained using the GSAS 2 EXPIGUI software. According to refinement data, we have for x0 (2-A) the values for X^2 of 1.69, Rwp (%) of 15.95 and Rp (%) of 12.64. For x20 (2-B) we have the values for X^2 of 2.63, Rwp (%) of 17.87 and Rp (%) of 13.42. For x80 (2-C) we have the values for X^2 of 2.760, Rwp (%) of 31.44 and Rp (%) of 42.45. For x100 (2-D) we have the values for X^2 of 3.011, Rwp (%) of 41.62 and Rp (%) of 29.43. According to the refines, it was possible to observe that the observed and theoretical values agree with the pattern of the diffractogram for the samples of synthesized $\text{Ni}_x\text{Cu}_{(1-x)}\text{Fe}_2\text{O}_4$ nanocrystals.

Figure 3 shows the morphologies of the samples obtained by SEM-FEG. In the samples that have a higher amount of copper, it is possible to verify irregular particles in size and shape. As for the samples with higher amounts of nickel, it is possible to verify the formation of triangles, which is a characteristic of the synthesis method, already identified by other authors^{15,18}.

The band gap is a crucial factor for any photocatalyst to work efficiently in a given optical range. UV-Vis diffuse reflectance spectroscopy is used to generate the energy gap of samples $\text{Ni}_x\text{Cu}_{(1-x)}\text{Fe}_2\text{O}_4$ (x0, x20, x80 and x100), with the aid of the Kubelka-Munk Equation (H) the absorption coefficient (α) is related to the reflectance (R), which is then related to the bandgap energy (E_{gap}) through the modified Tauc Equation (I).

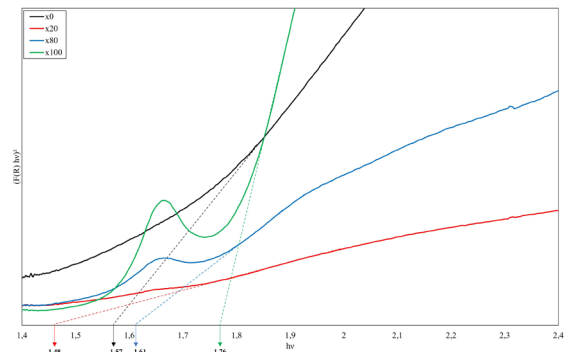


Figure 4. UV-Vis diffuse reflectance spectra measured at room temperature.

$$F(R) = \alpha = \frac{1(1-R)^2}{2R} \quad (\text{H})$$

$$F(R)hv = A(hv - E_{\text{gap}})^n \quad (\text{I})$$

Where n, denotes the direct ($n=2$) and indirect ($n=1/2$) energy gaps of the material. With these equations it is possible to plot the graph $(F(R)hv)^2$ vs hv (Figure 4) for all samples (x0, x20, x80 and x100), where it is possible to obtain the bandgap from the region with the highest slope of the curve, with the intersection of linear extrapolation of the curve on the energy axis¹⁹. The bandgap energy values obtained were 1.57 eV, 1.48 eV, 1.61 eV and 1.76 eV, for x0, x20, x80 and x100, respectively, presenting values similar to^{9,20}. Thus, the samples can absorb a considerable amount of light in the

visible region, due to the excitation of electrons from the valence band to the conduction band.

Semiconductor materials have had their conduction band (E_{CB}) and valence band (E_{VB}) positions calculated by empirical Equations (J) and (K)^{10,21}, and shown in Table 1.

$$E_{CB} = \chi - E^C - 0.5E_{gap} \quad (J)$$

$$E_{VB} = E_{CB} + E_{gap} \quad (K)$$

Where E_{CB} is the conduction band energy, E_{VB} is the valence band energy, χ is the absolute electronegativity of the material, and E^C is the energy of conduction electrons on the normal hydrogen scale (~4.5 eV).

From this, the formation of hydroxyl radicals occurs from photogeneration of the holes by the samples, oxidizing OH⁻ to generate •OH, due to the standard redox potential OH⁻/•OH being 1.99 eV (vs. NHE), being less than the valence band energy of all samples²²⁻²⁵.

The photocatalytic performance of Ni_xCu_(1-x)Fe₂O₄ samples (x0, x20, x80 and x100) were evaluated by degradation of rhodamine B dye at a concentration of 10 ppm, in the presence of air purge, under irradiation of visible light and pH variation. The substitution of metallic ions in the structure causes geometric and electronic changes in the structure, as evidenced in the characterizations made, which directly influence the degradation of the dye¹⁰. The pH is an important factor to be observed in the degradation of dyes, given that the effluents containing these compounds present large pH variations²⁶. Furthermore, the pH directly affects the surface properties of the catalysts, as well as the formation of hydroxyl radicals, and the dissociation of dye molecules²⁷.

Despite the photosensitizing character of Rhodamine B dye, when exposed only to lighting for a period of 240 minutes, concentration variations were not observed, as observed by²⁸. Thus, semiconductor materials act as accelerators of redox reactions, generating active species that promote the distillation of RhB, causing the peak to shift to blue, and consequently, the degradation of the dye at the end of the distillation processes^{10,29}.

Table 1. Ni_xCu_(1-x)Fe₂O₄ band energies.

	χ	E_{CB} (eV)	E_{VB} (eV)
CuFe₂O₄	5.852	0.567	2.137
Cu_{0.8}Ni_{0.2}Fe₂O₄	5.849	0.609	2.089
Cu_{0.2}Ni_{0.8}Fe₂O₄	5.84	0.535	2.145
NiFe₂O₄	5.837	0.457	2.217

Table 2. Values of apparent rate constants for Rhodamine B photodegradation under different pHs^{2,6,10} and different Ni_xCu_(1-x)Fe₂O₄ photometers (x0, x20, x80 and x100) in 240 min. under visible light irradiation.

	x0	x20	x80	x100
k (min⁻¹) for pH=2	0.0018	0.0012	0.0015	0.0009
k (min⁻¹) for pH=6	0.0016	0.0027	0.0017	0.0014
k (min⁻¹) for pH=10	0.0036	0.0033	0.0028	0.0016

The kinetic behavior of Ni_xCu_(1-x)Fe₂O₄ samples were investigated in order to quantitatively compare their photocatalytic activities. The degradation of rhodamine B, for all cases, resembled a first-order kinetics described by Equation (L), as also evidenced by^{8,10,30}, among others.

$$\ln\left(\frac{C}{C_0}\right) = kt \quad (L)$$

The variations of $\ln(C/C_0)$ were plotted as a function of time in order to obtain the kinetic velocity constants, which are shown in Table 2.

From Figure 5, it was verified that in acidic pH (pH = 2) the CuFe₂O₄ particles presented a better degradation, however for all samples: x0, x20, x80 and x100, the degradation percentages: 35.70%, 25.79%, 29.07%, 19.15%, respectively, were considered low due to the exposure time of 240 minutes. In Figure 6, a change in the behavior of the samples is identified

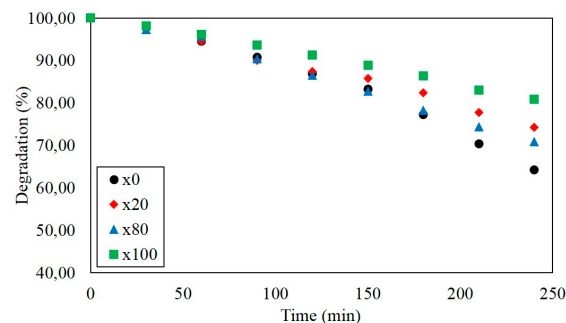


Figure 5. RhB photodegradation at pH=2 in the presence of x0, x20, x80 and x100.

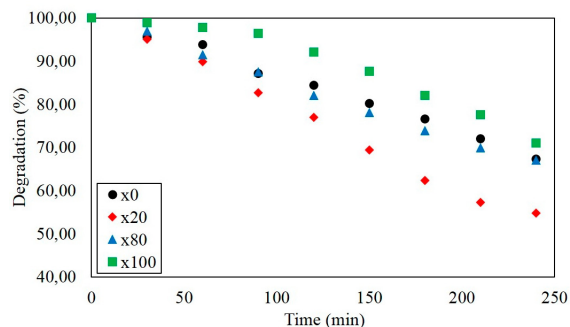


Figure 6. RhB photodegradation at pH=6 in the presence of x0, x20, x80 and x100.

due to the pH variation to 6, which may be directly related to the surface properties of the catalyst, where the sample x20 presented the best result, the degradation percentages were 32.72%, 45.27%, 32.93% and 28.92%, for x0, x20, x80 and x100, in order. And finally, in Figure 7 it is possible to verify that at the basic pH (pH = 10), that the samples with the highest percentage of copper (x0 and x20) were more prominent, as well as the degradation for all samples at that pH was improved, however, pure nickel ferrite did not show satisfactory results in any pH range. For pH=10, degradations of 54.87%, 53.36%, 48.04% and 32.38% were obtained for x0, x20, x80 and x100 in order.

Figure 8 illustrates the comparison between the degradations at different pHs, showing that the basic pH was better for the degradation of Rhodamine B with $\text{Ni}_x\text{Cu}_{(1-x)}\text{Fe}_2\text{O}_4$, as shown in Figure 7 and according to the constants of speed obtained in Table 2.

From this it is identified that the degradation of rhodamine B by heterogeneous photocatalysis using copper and nickel ferrites as a catalyst, occurs more effectively in a basic medium, with the pH influencing the surface of the catalyst as well as on the dissociation of the molecules of the dye. Catalysts containing a higher percentage of copper (x0, x20) showed superior results in all tests, thus being considered better for this purpose. Linked to this, the sample containing only nickel obtained the least favorable results at all pH's, proving that copper plays an important role in the property of photocatalytic degradation.

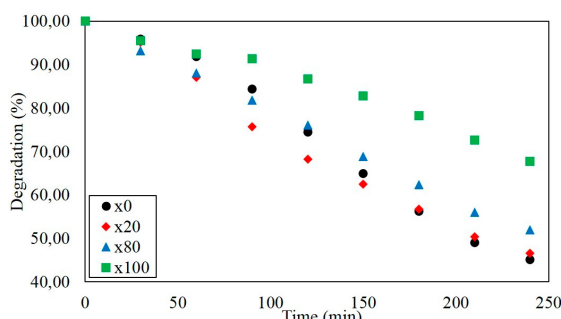


Figure 7. RhB photodegradation at pH=10 in the presence of x0, x20, x80 and x100.

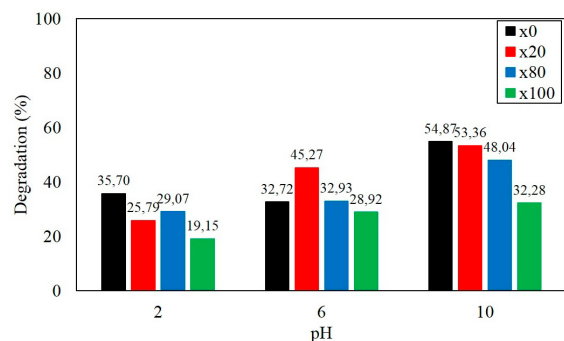


Figure 8. Effects of pH variation on RhB degradation by heterogeneous photocatalysis using $\text{Ni}_x\text{Cu}_{(1-x)}\text{Fe}_2\text{O}_4$.

4. Conclusion

$\text{Ni}_x\text{Cu}_{(1-x)}\text{Fe}_2\text{O}_4$ nanoparticles were successfully produced by the EDTA-Citrate method, generating a crystalline material with good bandgap energy values that attribute to their potential photocatalyst properties. According to the presented results, it is noticed that there is an influence of pH on the action of nickel and copper ferrites in the degradation of Rhodamine B and that the samples with higher copper contents CuFe_2O_4 and $\text{Ni}_{0.2}\text{Cu}_{0.8}\text{Fe}_2\text{O}_4$ showed better results in all pH ranges studied. As well as the NiFe_2O_4 sample, which contains only nickel, it proved to be the least efficient in all pH ranges, showing that copper plays an important role in the performance of copper and nickel ferrites as photocatalysts.

5. Acknowledgments

The authors acknowledge CAPES/Brazil (Finance Code 001) for their financial support and the post graduate program in Chemical Engineering (PPGEQ).

6. References

1. Tkaczyk A, Mitrowska K, Posyniak A. Synthetic organic dyes as contaminants of the aquatic environment and their implications for ecosystems: a review. *Sci Total Environ.* 2020;717:137222.
2. Al-Buriah AK, Al-Gheethi AA, Senthil Kumar P, Radin Mohamed RMS, Yusof H, Alsharif AF, et al. Elimination of rhodamine B from textile wastewater using nanoparticle photocatalysts: a review for sustainable approaches. *Chemosphere.* 2022;287:132162.
3. Chequer FMD, Oliveira GAR, Ferraz ERA, Cardoso JC, Zanoni MVB, Oliveira DP. Textile dyes: dyeing process and environmental impact [Internet]. In: Günay M, editor. Eco-friendly textile dyeing and finishing. London: IntechOpen; 2013 [cited 2023 Jan 16]. Available from: <https://www.intechopen.com/chapters/41411>
4. Alaton IA, Balcioğlu IA, Bahnemann DW. Advanced oxidation of a reactive dye bath effluent: comparison of O_3 , $\text{H}_2\text{O}_2/\text{UV-C}$ and TiO_2/UV : a processes. *Water Res.* 2002;36(5):1143-54.
5. Henderson MA. A surface science perspective on TiO_2 photocatalysis. *Surf Sci Rep.* 2011;66(6-7):185-297.
6. Nogueira RFP, Jardim WF. A fotocatalise heterogênea e sua aplicação ambiental. *Quim Nova.* 1998;21(1):69-72.
7. Kharisov BI, Dias HVR, Kharisova OV. Mini-review: ferrite nanoparticles in the catalysis. *Arab J Chem.* 2019;12(7):1234-46.
8. Sundararajan M, Sailaja V, John Kennedy L, Judith Vijaya J. Photocatalytic degradation of rhodamine B under visible light using nanostructured zinc doped cobalt ferrite: kinetics and mechanism. *Ceram Int.* 2017;43(1, Suppl. 1, Part A):540-8.
9. Gayathri Manju B, Raji P. Biological synthesis, characterization, and antibacterial activity of nickel-doped copper ferrite nanoparticles. *Appl Phys, A Mater Sci Process.* 2019;125(5):313.
10. Dhiwaha AT, Maruthamuthu S, Marnadu R, Sundararajan M, Manthrammel MA, Shkir M, et al. Improved photocatalytic degradation of rhodamine B under visible light and magnetic properties using microwave combustion grown Ni doped copper ferrite spinel nanoparticles. *Solid State Sci.* 2021;113:106542.
11. Rao P, Godbole RV, Bhagwat S. Copper doped nickel ferrite nano-crystalline thin films: a potential gas sensor towards reducing gases. *Mater Chem Phys.* 2016;171:260-6.
12. Zhao H, Zheng Z, Wong KW, Wang S, Huang B, Li D. Fabrication and electrochemical performance of nickel ferrite nanoparticles as anode material in lithium ion batteries. *Electrochem Commun.* 2007;9(10):2606-10.
13. Naz K, Khan JK, Khalid M, Akhtar MS, Gilani ZA, Noor ul Huda Khan Asghar HM, et al. Structural, dielectric, impedance

- and electric modulus analysis of Ni substituted copper spinel ferrites nanoparticles for microwave device applications. *Mater Chem Phys*. 2022;285:126091.
14. Hong Y, Ren A, Jiang Y, He J, Xiao L, Shi W. Sol-gel synthesis of visible-light-driven Ni_(1-x)Cu_(x)Fe₂O₄ photocatalysts for degradation of tetracycline. *Ceram Int*. 2015;41(1, Suppl. 1, Part B):1477-86.
 15. Rodrigues MV. Síntese e caracterização de ferritas mistas de níquel e cobre pelo método de complexação combinado EDTA/Citrato [dissertation]. Natal: Universidade Federal do Rio Grande do Norte; 2020 [cited 2023 Jan 16]. Available from: <https://repositorio.ufrn.br/handle/123456789/30701>
 16. Patra H, Rout SK, Pratihari SK, Bhattacharya S. Effect of process parameters on combined EDTA-citrate synthesis of Ba_{0.5}Sr_{0.5}Co_{0.8}Fe_{0.2}O_{3-δ} perovskite. *Powder Technol*. 2011;209(1-3):98-104.
 17. Davis ME, Davis RJ. *Fundamentals of chemical reaction engineering*. Massachusetts: Courier Corporation; 2012. 385 p.
 18. Silva MMS, Raimundo RA, Silva TR, Araújo AJM, Macedo DA, Morales MA, et al. Morphology-controlled NiFe₂O₄ nanostructures: influence of calcination temperature on structural, magnetic and catalytic properties towards OER. *J Electroanal Chem*. 2023;933:117277.
 19. Yousaf M, Noor A, Xu S, Akhtar MN, Wang B. Magnetic characteristics and optical band alignments of rare earth (Sm⁺³, Nd⁺³) doped garnet ferrite nanoparticles (NPs). *Ceram Int*. 2020;46(10, Suppl. 10, Part B):16524-32.
 20. Ghosh MP, Datta S, Sharma R, Tanbir K, Kar M, Mukherjee S. Copper doped nickel ferrite nanoparticles: Jahn-Teller distortion and its effect on microstructural, magnetic and electronic properties. *Mater Sci Eng B*. 2021;263:114864.
 21. Zhou Y, Wang Y, Wen T, Zhang S, Chang B, Guo Y, et al. Mesoporous Cd_{1-x}Zn_xS microspheres with tunable bandgap and high specific surface areas for enhanced visible-light-driven hydrogen generation. *J Colloid Interface Sci*. 2016;467:97-104.
 22. Jarusheh HS, Yusuf A, Banat F, Haija MA, Palmisano G. Integrated photocatalytic technologies in water treatment using ferrites nanoparticles. *J Environ Chem Eng*. 2022;10(5):108204.
 23. Xu Y, Liu Q, Xie M, Huang S, He M, Huang L, et al. Synthesis of zinc ferrite/silver iodide composite with enhanced photocatalytic antibacterial and pollutant degradation ability. *J Colloid Interface Sci*. 2018;528:70-81.
 24. Behera A, Kandi D, Majhi SM, Martha S, Parida K. Facile synthesis of ZnFe₂O₄ photocatalysts for decolourization of organic dyes under solar irradiation. *Beilstein J Nanotechnol*. 2018;9(1):436-46.
 25. Pattnaik SP, Behera A, Martha S, Acharya R, Parida K. Synthesis, photoelectrochemical properties and solar light-induced photocatalytic activity of bismuth ferrite nanoparticles. *J Nanopart Res*. 2018;20(1):10.
 26. Deng Y, Zhao R. Advanced Oxidation Processes (AOPs) in wastewater treatment. *Curr Pollut Rep*. 2015;1(3):167-76.
 27. Nagaraja R, Kottam N, Girija CR, Nagabhushana BM. Photocatalytic degradation of Rhodamine B dye under UV/solar light using ZnO nanopowder synthesized by solution combustion route. *Powder Technol*. 2012;215-216:91-7.
 28. Wu T, Liu G, Zhao J, Hidaka H, Serpone N. Photoassisted degradation of dye pollutants. V. self-photosensitized oxidative transformation of rhodamine B under visible light irradiation in aqueous TiO₂ dispersions. *J Phys Chem B*. 1998;102(30):5845-51.
 29. Li W, Li D, Meng S, Chen W, Fu X, Shao Y. Novel approach to enhance photosensitized degradation of Rhodamine B under Visible Light Irradiation by the Zn_xCd_{1-x}S/TiO₂ Nanocomposites. *Environ Sci Technol*. 2011;45(7):2987-93.
 30. Li Y, Sun S, Ma M, Ouyang Y, Yan W. Kinetic study and model of the photocatalytic degradation of rhodamine B (RhB) by a TiO₂-coated activated carbon catalyst: effects of initial RhB content, light intensity and TiO₂ content in the catalyst. *Chem Eng J*. 2008;142(2):147-55.